Lipidic folding pathway of α-Synuclein via a toxic oligomer

Christian Griesinger

cigr@nmr.mpibpc.mpg.de

Max Planck Institute for Multidisciplinary Sciences https://orcid.org/0000-0002-1266-4344

Vrinda Sant

Max Planck Institute for Multidisciplinary Sciences

Dirk Matthes

Max Planck Institute for Multidisciplinary Sciences

Hisham Mazal

Max Planck Institute for the Science of Light https://orcid.org/0000-0002-2071-9552

Leif Antonschmidt

Max Planck Institute for Multidisciplinary Sciences

Franz Wieser

Max Planck Institute for the Science of Light

Kumar Movellan

Max Planck Institute for Multidisciplinary Sciences

Kai Xue

MPINAT

Evgeny Nimerovsky

Max Planck Institute for Multidisciplinary Sciences

Marianna Stampolaki

Max Planck Institute for Multidisciplinary Sciences https://orcid.org/0000-0002-0144-4792

Magdeline Nathan

Max Planck Institute for Multidisciplinary Sciences

Dietmar Riedel

Max Planck Institute for Biophysical Chemistry

Stefan Becker

Max Planck Institute for Multidisciplinary Sciences https://orcid.org/0000-0003-2041-5740

Vahid Sandoghdar

Max Planck Institute for the Science of Light https://orcid.org/0000-0003-2594-4801

Bert de Groot

Max-Planck Institute for Multidisciplinary Sciences

Loren Andreas

Max Planck Institute for Biophysical Chemistry https://orcid.org/0000-0003-3216-9065

Article

Keywords:

Posted Date: June 4th, 2024

DOI: https://doi.org/10.21203/rs.3.rs-4437173/v1

Additional Declarations: There is **NO** Competing Interest.

Lipidic folding pathway of α-Synuclein via a toxic oligomer

Vrinda Sant[1], Dirk Matthes[2], Hisham Mazal[3], Leif Antonschmidt[1], Franz Wieser[3], Kumar T. Movellan[1]†, Kai Xue[1]‡, Evgeny Nimerovsky[1], Marianna Stampolaki[1], Magdeline Nathan[1], Dietmar Riedel[4], Stefan Becker[1], Vahid Sandoghdar[3], Bert L. de Groot[2*], Christian Griesinger[1,5*], Loren B. Andreas[1*]

[1]NMR based Structural Biology, Max Planck Institute for Multidisciplinary Sciences; Göttingen, Germany.

[2]Department of Theoretical and Computational Biophysics, Max Planck Institute for Multidisciplinary Sciences; Göttingen, Germany.

[3]Max Planck Institute for Science of Light; Erlangen, Germany.

[4]Facility for Electron Microscopy, Max Planck Institute for Multidisciplinary Sciences; Göttingen, Germany.

[5]Cluster of Excellence "Multiscale Bioimaging: From Molecular Machines to Networks of Excitable Cells" (MBExC), University of Göttingen; Göttingen, Germany.

*Corresponding authors. Email: cigr@mpinat.mpg.de, land@mpinat.mpg.de, bgroot@mpinat.mpg.de

†Current address: Brown Laboratory, Department of Chemistry and Biochemistry, University of Delaware; Newark, Delaware, USA.

‡Current address: Center of High Field Imaging, Nanyang Technological University, 637371, Singapore

Summary

Aggregation intermediates play a pivotal role in the assembly of amyloid fibrils, which are central to the pathogenesis of neurodegenerative diseases[1,2]. The structures of filamentous intermediates[3] and mature fibrils[4] are now efficiently determined by single-particle cryo-electron microscopy. By contrast, smaller pre-fibrillar α-Synuclein (αS) oligomers, crucial for initiating amyloidogenesis, remain largely uncharacterized. We report an atomic-resolution structural characterization of a toxic pre-fibrillar aggregation intermediate (I1) on pathway to the formation of lipidic fibrils. Super-resolution microscopy reveals a tetrameric state, providing insights into the early oligomeric assembly. Time resolved nuclear magnetic resonance (NMR) measurements uncover a structural reorganization essential for the transition of I1 to mature lipidic L2 fibrils. The reorganization involves the transformation of anti-parallel β-strands during the pre-fibrillar I1 state into a β-arc characteristic of amyloid fibrils. This structural reconfiguration occurs in a conserved structural kernel shared by a vast number of αS-fibril polymorphs including extracted fibrils from Parkinson's and Lewy Body Dementia [5] patients. Consistent with reports of anti-parallel β-strands being a defining feature of toxic αS pre-fibrillar intermediates[6], I1 impacts viability of neuroblasts and disrupts cell membranes, resulting in an increased calcium influx. Our results integrate the occurrence of anti-parallel β-strands as unique features of toxic oligomers[7–9] with their significant role in the amyloid fibril assembly pathway. These structural insights have implications for the development of therapies and biomarkers.

Introduction

The aberrant aggregation of α-Synuclein (αS) into amyloid fibrils is a crucial step in the biochemical cascade of several neurodegenerative diseases (NDD) as evidenced by the fact that αS amyloid fibrils are a major component of Lewy bodies, the intra-cellular inclusions that are characteristic of Parkinson's disease and other synucleinopathies [1,10]. While fibrils are a pathological hallmark of NDDs, evidence has accumulated that oligomeric αS aggregation intermediates, in particular, exert a toxic load on neurons [11–14]. Further, the ability of αS to interact with and disrupt lipid bilayers is well documented [8,11,15]. Hence, such structures in complex with lipids, a canonical binding partner of αS[16–19], are of particular interest.

In vitro preparations have been instrumental in determining characteristics of intermediate species occurring during amyloid aggregation because their low population and transient nature make it challenging to isolate from tissues. Through these studies it has been revealed that aggregation intermediates, sometimes transient fibril like filaments[3], are often composed of segments with structural features analogous to their respective fibrillar polymorphs[20–23]. However, atomic-resolution structures of small oligomeric αS intermediates are lacking. This impedes the understanding of nucleation, toxicity, and the effect of aggregation modulators at the molecular level.

Previously, we reported the isolation of Intermediate 1 (I1), a transient pre-fibrillar species found on pathway to the formation of the L2 fibril polymorph (Protein Data Bank (PDB) entry 8A4L) in the presence of anionic lipid vesicles [23,24] (Fig.1A). Nuclear Magnetic Resonance (NMR) chemical shifts indicated that I1 shares several segments with the L2 fibril, including residues L38-S42 in β1, T44-V48 in loop 1, E57-E61 in loop 2, T72-A78 in loop 3 and β4[23] (Fig.1D, E).

A β-arc, which is a characteristic feature of amyloid fibrils, is found at T59 (V52-V66) in the L2 fibril. This β-arc is a structural kernel conserved in nearly half of the deposited αS fibril polymorphs (Fig.1B), including extracted fibrils from Parkinson's disease (PD) and Lewy Body Dementia (DLB) patients (PDB 8A9L) and those seeded from Multiple System Atrophy (MSA) (PDB 7NCA) and PD patients (PDB 7OGZ). Determination of the structure of I1, which clearly differs from the fibril for residues V52-V66 (Fig.1A, D, E)[23], would help elucidate the folding pathway for L2, thus far unknown[7,13].

Here, we report extensive NMR data for I1 that reveal an anti-parallel β-sheet with a β-hairpin at T59. Together with super-resolution fluorescence microscopy data, I1 was determined to be a tetramer. Atomistic molecular dynamics (MD) simulations reveal that the tetramer is stabilized in the context of a lipid bilayer.

Results

Composition and stability of an I1 sample

The characterization of an I1 sample, previously isolated on the folding pathway to the L2 fibril[23], reveals its prolonged stability and composition. The I1 sample can be isolated for prolonged times in the rotor because it is depleted of disordered monomer and membrane bound monomer (Fig.1A). Fingerprint spectra are acquired at regular intervals to keep track of

the stability of I1 (Fig.S1A). Lipid bound monomer and disordered monomer stay in the supernatant after I1 is isolated (Fig.S1B, C). Due to its transient nature, multiple freshly prepared samples of I1 have been used in the study (Fig.S1E). The spectra indicate that I1 consists of one dominant species (Fig.S1, S2). Additionally, there was no indication of the L2 fibril in the I1 samples, as determined by the absence of characteristic L2 resonances in the I1 spectra (Fig.S1). Notably, no instance occurred where one residue was assigned to two sets of resonances (Fig.S2).

I1 is toxic to SH-SY5Y neuroblasts

Consistent with well-established behavior of amyloid aggregates[8,14], I1 and the L2 fibril dramatically differ in their impact on cell viability: I1 reduces survival of SH-SY5Y neuroblastoma cells to 25%, while the L2-fibril leaves cell viability unperturbed compared to the lipid bound monomer (Fig.1C). This is despite the remarkable similarity between the two species and further motivates a detailed characterization to link structural differences to variations in cellular impacts.

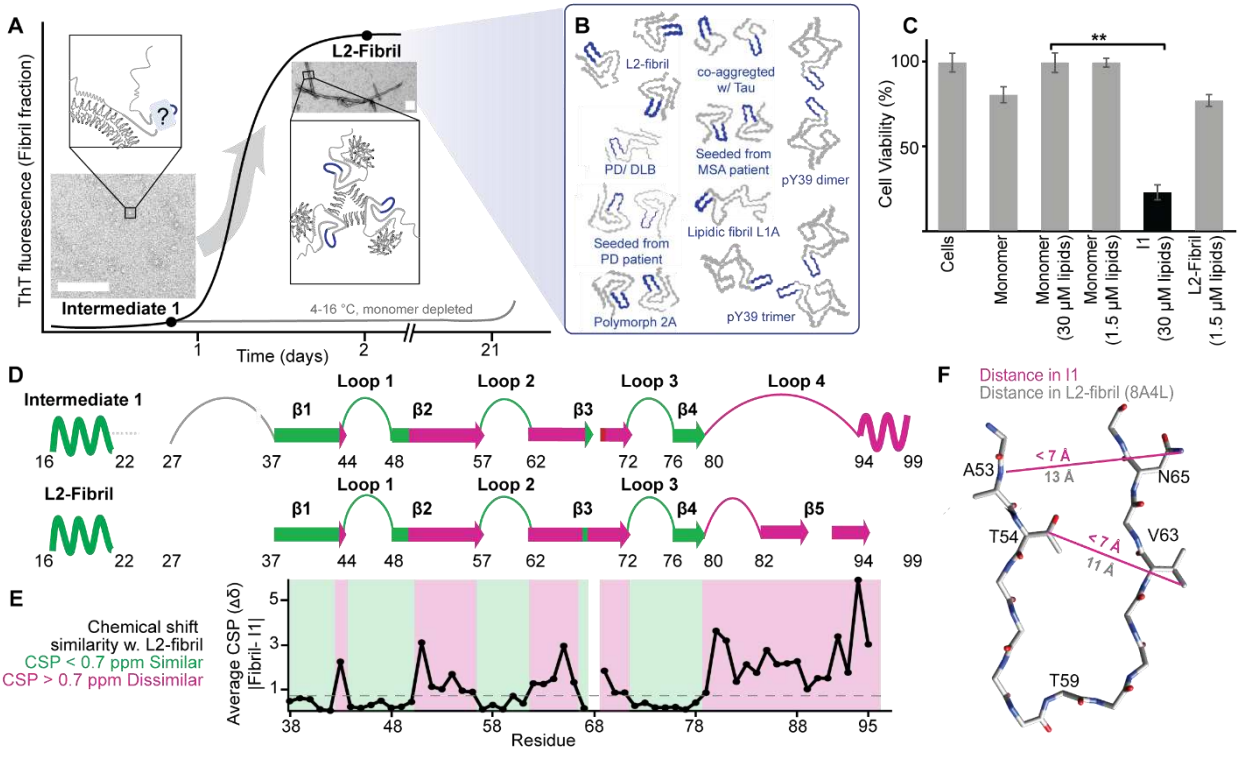

Figure1: **Comparison of I1 oligomer and L2 fibril.** (A) Transmission electron micrograph (TEM) image of I1 aggregates (left) compared to a TEM image of L2 fibrils (right) superimposed on an aggregation kinetics curve (black curve). Insets show schematics of structures and highlight unknown aspects of I1. Scale bar 100 nm. The schematic shows lipid

localization as previously determined[25]. The gray curve shows slower aggregation kinetics under conditions during NMR measurements (4-16°C and monomer depleted). (B) Backbone traces of αS fibril polymorphs that have a β-arc at T59 similar to the L2 fibrils. (C) Impact of αS aggregates on viability of SH-SY5Y neuroblastoma cells after 24 hours of incubation with 0.3 μM αS. Error bars are shown as the ± standard error of the mean for 6 replicates. ** represents significance from *t*-test $p < 0.05$ between the monomer and I1 samples. (D) The secondary structure as indicated by chemical shift, is shown as helix (waves), strand (arrows) or loops (lines) for Intermediate 1 (I1) and the L2 fibril. Chemical shift similarity (green-pink) mapped onto the sequence of αS. Dotted lines represent tentative assignments. White spaces indicate missing assignments. Gray lines denote assigned residues of I1 that are unassigned in the L2 fibril. (E) Per residue average chemical shift perturbations (CSPs), including Cα, Cβ, Co and N_H shifts, between I1 and L2 fibril (BMRB 50585) mapped along the αS primary sequence. Dotted line shows the 0.7 ppm cut-off for similar and dissimilar segments. (D-E) Residues with similar chemical shifts (CSPs <0.7 ppm) are colored green. Residues with dissimilar chemical shifts (CSP >0.7 ppm) are pink. Similarity for the helical segment V16-T22 is derived from ^{13}C correlation spectra only[23]. (F) Side-chain contacts observed for I1 (from (H)HNH and (H)HCH spectra in Fig.S3B) conflicting with the L2 fibril structure (grey trace) are marked in pink.

Distinct features of I1 compared to the L2 fibril

Clear differences are seen between I1 and the L2 fibril in morphology as well as secondary structure and topology. An I1 sample resolubilized from an MAS NMR rotor consists of particles of diameter 8-15 nm, drastically different from longitudinal, twisted strands observed for fibrils (Fig.1A). Comparison of Cα and Cβ chemical shifts (BMRB entries 50585[23] and 52283) reveals major differences between I1 and L2 in two regions of αS. Firstly, C-terminal residues, E83-K97, that are primarily structured as a β-strand in the L2 fibril, form a loop and α-helix in I1 (Fig.1D). Differences in topology are also observed in this segment: K96 shows contacts to residues around A30 in I1. By contrast, residues V82-L97 are adjacent to β3 in the L2 fibril (Fig.S3B, C). Secondly, the β2 and β3 strands, while retaining β-strand secondary structure in both, I1 and the L2 fibril (Fig.1D), deviate substantially in their chemical shifts (average CSP >0.7 ppm) (Fig.1E). These segments exhibit side-chain contacts in I1, that conflict with the L2 fibril, namely N65 N_δ – A53 H_N and V63 H_γ – T54 H_β, (Fig.1F). In the L2 fibril these contacts measure greater than 10 Å, which is beyond the

147 distance reached in H(H)NH NMR spectra. In the L2 fibril, β2 and β3 form the T59 β-arc, a
148 shared structural kernel among various fibril polymorphs, suggesting possible commonalities
149 in the folding pathway of other fibrils sharing the T59 β-arc.

150 To determine the β-strand arrangement in I1, we recorded amide proton correlation
151 spectra[26] on the 1.2 GHz spectrometer to leverage improved resolution and sensitivity
152 (Fig.S3A). Parallel-in-register (PIR) and anti-parallel (AP) β-strands produce distinct contact
153 maps of proximity among amide moieties. β1 and β4 are confirmed as PIR, since only
154 correlations to neighboring residues are observed (green labels, for example K43-T44 in Fig.
155 2A). In contrast, the pattern of amide proton correlations for β2 and β3 reveals an AP
156 arrangement (pink labels in Fig 2A). These correlations for V52-V55 on β2 with V66-V63 on
157 β3 are depicted in Fig.2B. To distinguish intra- and inter- molecular amide proton contacts,
158 we diluted the uniformly ^{15}N-labelled αS with 50% unlabelled αS. Once normalized by the
159 diagonal, the intensities of inter-molecular contacts in the diluted labelling spectrum (blue,
160 Fig.2A) are reduced 2-fold compared to the fully labelled spectrum (black, Fig.2A), while
161 intramolecular contacts retain full intensity. In this way we identified the V66-V52 (AP) and
162 K43-T44 (PIR) cross-peaks as inter-molecular whereas the V63-V55 cross-peak was
163 identified as intramolecular (Fig.2C).

164

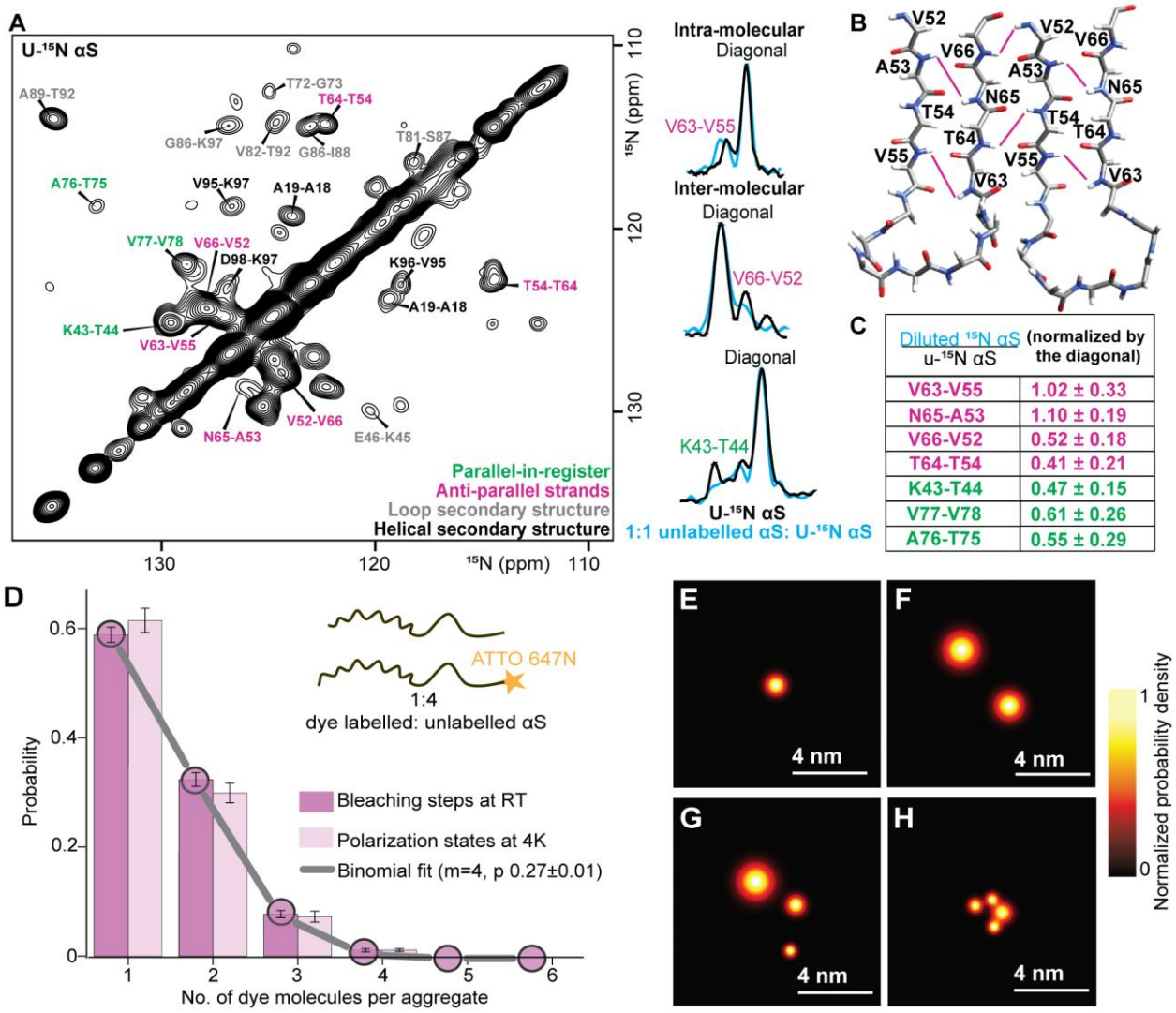

Figure 2: I1 has inter- and intra- molecular (AP) β-strands and is a tetramer. (A) ^{15}N-^{15}N correlation spectrum of I1 with uniformly ^{15}N- labelled αS shows that there are AP segments (pink labels) which feature intra- and inter-molecular cross-peaks. Cross-peaks from PIR segments (green labels), correlations in loops (grey labels) and helices (black labels) are also observed. On the right are one-dimensional traces of cross-peaks comparing uniformly ^{15}N-labelled I1 (black) and 1:1 ^{15}N: unlabelled (50% dilute) I1 (blue). Intra-molecular cross-peaks are not affected by the 50% dilution (V63-V55 contact) whereas the intensity of inter-molecular cross-peaks is reduced 2-fold in the diluted spectrum (blue) (V66-V52 and K45-T44 contacts). (B) Contacts indicative of AP segments are indicated with pink lines on a backbone trace. (C) Ratios of cross-peak intensity between the fully ^{15}N-labeled (black) and 50% ^{15}N-labeled (blue) spectra. Color legend is the same as in panel (A). (D) Histograms of the number of bleaching steps (purple) and number of polarization states per aggregate (pink) for I1 at a fluorophore labelling efficiency (p) of 25%. The grey line shows the best fit to the photobleaching and polarCOLD data with parameters p =27% and m (no. of monomers per

oligomer) =4 (Fig.S4F). (E-H) Examples of super-resolved polarCOLD images of different particles show the projection of aggregates with 1 (E), 2 (F), 3 (G) and 4 (H) dye molecules onto the imaging plane. The center of each spot displays the position of the fluorophore and its width represents the localization precision. The latter can vary due to the available signal-to-noise in each case, determined by the photophysics heterogeneity of fluorophores (Fig.S4G).

Oligomer state of I1

Amide proton correlations indicate that I1 is a multimer, prompting further investigation with NMR and fluorescence measurements to determine oligomer size. An NMR CODEX[27] (Center band only detection of exchange) measurement informs about the monomer number in an aggregate with an upper limit of about 10 Å between singly ^{13}C-labeled sites. The CODEX curve reaches about 0.25 at long times, indicating that I1 is at least a 4-mer (Fig.S4A). Stepwise photobleaching can be used to count the number of monomers in an aggregate[28]. In this work, we combine this approach with polarCOLD, a cryogenic super-resolution fluorescence microscopy, which can reach Ångstrom resolution[29]. We first verified that modification of a portion of molecules in I1 with a fluorophore showed no perturbations in NMR structural data (Fig.S4C). Next, aggregates were immobilized on a substrate and irradiated continuously at room temperature (RT) until they photobleached (Fig.S4D). The number of photobleaching steps was determined by counting the intensity levels in the time-traces (Fig.S4E). The histogram of photobleaching steps at RT can be best fit to a binomial distribution for a tetramer (purple, Fig.2D). Furthermore, polarCOLD [30], was used to acquire super-resolution images at a temperature of 4 K by localizing individual fluorophores through their emission polarization states. Examples of such images for the projection of fluorophore positions are depicted in Fig.2E-H for different particles from a single preparation of I1 with ~ 27% dye labeling. We also analyzed an ensemble of individual particles to obtain a histogram of polarization states per aggregate at 4 K (pink in Fig.2D), yielding very good agreement with the RT measurements. These measurements all indicate that I1 is a tetramer.

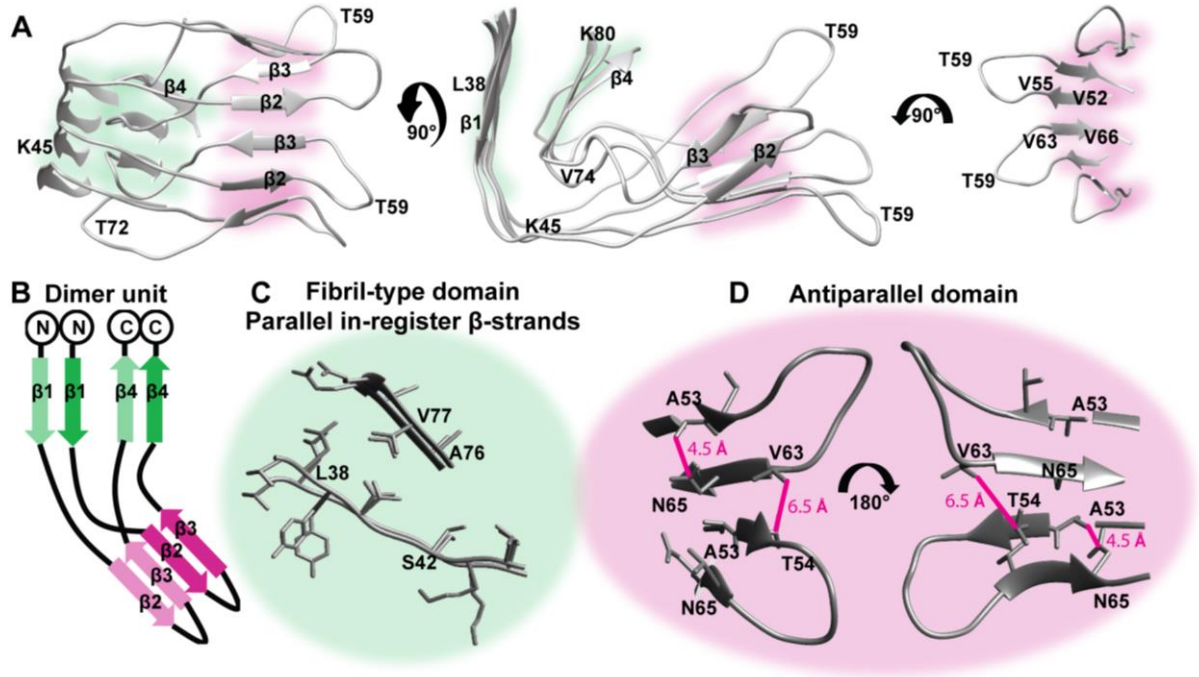

Figure 3: I1 fold contains AP β-structure and PIR strands. (A) Tetramer with open AP β-strands 2 and 3 and (B) Schematic of a dimeric structural element of the tetramers. The fibril-like PIR domain is colored green. The AP domain is colored pink. (*C*) Close up of the PIR part. (D) Close up of the AP arrangement showing the contacts N65 N_{δ}–A53 H_N and V63 H_{γ}–T54 H_{β} as pink lines. The structure satisfies an upper limit of 7 Å.

Visualization of the I1 tetramer structure

An atomic resolution model for an I1 tetramer was assembled by combining the knowledge of the L2 fibril structure (for I1 segments similar to the fibril) with experimental contacts observed for I1 that are distinct from the L2 fibril (Table S1). Detection of a single set of chemical shifts suggests a single fold for all monomers of I1, but several quaternary arrangements can be modeled to satisfy experimental restraints (Fig. S5). These include "open" arrangements where molecules simply stack on each other like in the fibril (Fig.3A). We can envisage "closed" arrangements, such as a "barrel" with inter-molecular H-bonds for all four molecules or a "bowl" morphology with intra-molecular H-bonds for all molecules except one (Fig. S5A). A comparison of the conformers reveals two distinct structural features in all morphologies (Fig.3B, C, Fig. S5A). The first is a ***fibril-like PIR*** arrangement of β1 and β4 (green, Fig.3). The second is an ***AP domain*** that involves a β-hairpin between strands β2 and β3 connected by loop 2 (pink, Fig.3). The AP domain in both open and closed models satisfies the 7 Å upper-limit for side-chain contacts in I1 (Fig.3D).

Transition from β-hairpin in I1 to β-arc is necessary for formation of the L2 fibril

To convert to the L2 fibril, I1 must undergo a transition in the AP domain from a β-hairpin, with backbone H-bonds between β2 and β3, to a β-arc with side-chain interactions between β2 and β3 instead. The kinetic stability of I1 is partly attributed to the relatively high energy barrier required for breaking 28 H-bonds involved in this transition (Movie S1). Contrary to an amyloid fibril, an I1 type conformation cannot template an indefinite number of molecules. Every additional molecule that contributes one layer to the PIR domain, adds two layers to the AP domain. This causes frustration between the two domains in larger aggregates and manifests as steric clashes in the G67-V74 segment and discontinuities in AP β-strands (Fig.S5B), making it energetically unfavorable to template both the AP and PIR domain onto additional molecules (Fig.S5C).

This is consistent with the finding that Intermediate 2 (I2), the next intermediate on the pathway, features a β-arc in the V52-V66 segment, and thus a conversion from AP to PIR β-strands in this region, indicated by similar chemical shifts to the L2 fibril [23] and next neighbor correlations in the amide proton correlation spectrum (Fig.S6A). Characteristic of fibrillar intermediates, I2 exhibits filamentous morphology (Fig.S6B) and coincides with a rapid increase in ThT fluorescence (Fig.S6C) indicating fibril growth through the necessary transition from β-hairpin between the AP β-strands in I1 to β-arc between the parallel β-strands.

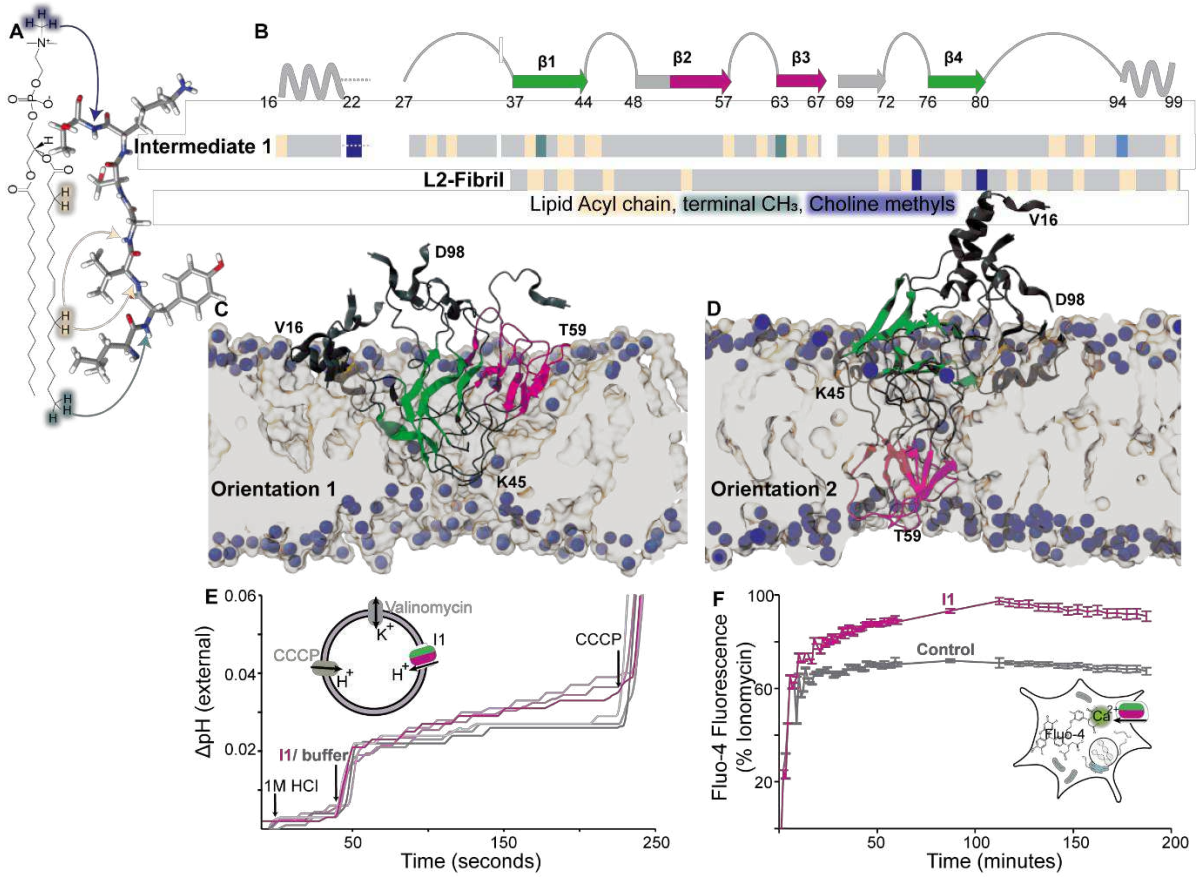

Figure 4: PIR and AP domains of I1 are lipid bound and disrupt lipid membranes (A) Schematic of magnetization transfer between lipid protons and protein backbone. POPC choline nitrogen atoms are highlighted in purple, terminal methyl groups in the hydrophobic core are turquoise and acyl chain protons are light orange. (B) lipid contacts mapped onto the sequence for I1 and the L2 fibril[23]. Lipid contacts are colored according to lipid protons in panel (*A*) and are shown together with a schematic of the I1 secondary structure along its sequence. The PIR domain is colored green, and the AP domain is pink. Residues with missing assignments are shown as white spaces and those with tentative assignments are shown as dotted lines. (C, D) Snapshots from unrestrained MD simulations of an open I1 conformer with (C) both PIR and AP domains being in the same leaflet and (D) PIR and AP domains traversing both leaflets of the bilayer. POPC choline nitrogen atoms are shown as purple spheres along with a surface map of lipids. I1 is shown as a gray ribbon colored by domain as in panel *(B)*. (E) I1induces proton flux across liposome membranes. Adding 1 M HCl lowers the pH of the external buffer. When I1 is introduced, the pH gradually increases (pink traces), indicating a leaky membrane. Without I1 (gray traces), the pH remains nearly unchanged until the addition of CCCP to uncouple proton flux. The inset shows a schematic of liposomes used in the assay. (F) Calcium influx is measured by fluorescence of Fluo-4 loaded in SH-SY5Y cells, expressed as a percentage of the maximum capacity determined by

cells containing ionomycin, a calcium ionophore. I1(pink) significantly elevates intracellular calcium levels compared to controls (gray). Error bars represent standard error of the mean. Inset illustrates Ca^{2+} flux induced by I1.

Interaction of I1 with lipids

I1 has lipid interactions spanning the entire length of the protein, consistent with its aggregation on POPC/POPA vesicles[23], (Fig.4A, B and Fig.S7). This includes the N-terminal helix and hydrophobic residues 70-88 (Fig.4B, S7) consistent with previously observed αS oligomers [11]. Additionally, I1 also contacts lipids through Y39 and through the AP domain. The lipid contacts at Y39 are similar in the L2 fibril and I1, while L2 type lipid contacts at β4 are missing in I1.

All-atom MD simulations were performed to probe interactions of I1 with lipid bilayers. Simulations of several orientations of I1 with respect to bilayers with a truncated G36-K80 segment identified orientations compatible with experimental lipid contacts (Supplementary Note 1, Fig.S8). Simulations that include the helical regions (V16-Q99), predict that the open morphology in orientations 1 and 2 and the bowl morphology in orientation 2 satisfy experimentally observed lipid contacts and distance restraints with high fidelity (Fig.4C, D and Fig.S9).

Lipids appear to play a crucial role in stabilizing the AP domain. The E57-V66 segment in the AP domain contacts lipids in I1 (Fig.4B), while in the L2 fibril, this segment forms a PIR β-sheet and does not show any lipid contacts. Notably, MD simulations of I1 with the AP domain oriented outside the lipid bilayer do not agree with experimental restraints and show a significant loss in β-strand content (orientations 3, and 5-8 in Fig.S8 and orientation 3 in Fig.S9).

I1 disrupts membranes

Strikingly, a cluster of charged residues in loop 1 (43KTKE46) and the AP domain (57EKTKEQ62) of I1 has contacts with lipid acyl chains (Fig.4B). Simulations of the open tetramer show that lipid bending stabilizes these residues (Fig. 4C, D and Movies S2, 3), reducing the energy barrier for the penetration of choline and phosphate groups of the lipid headgroups into the bilayers hydrophobic core (Fig.S10A-D). This lipid bending also

facilitates cation flux across the membrane by lowering the energy barrier for Na^+, Ca^{2+} and water in the hydrophobic bilayer core (Fig.S10A-D).

The disruptive impact of I1 on lipid membranes is evident from the liposomal proton flux assay. After establishing a pH gradient across the membrane by the addition of an acid, I1 triggers a proton influx into liposomes, gradually increasing the pH of the external buffer (Fig.4E). By contrast, in the absence of I1, liposomes are sealed and maintain a stable pH. Furthermore, I1 increases Ca^{2+} influx across neuroblast cell membranes, as indicated by the enhanced fluorescence of the calcium sensitive dye, Fluo-4 (Fig.4F). Propidium Iodide fluorescence confirms that increased Fluo-4 fluorescence is not due to cell death induced membrane damage (Fig.S10E). Unlike with I1, both monomeric and fibrillar αS show no significant differences in Ca^{2+} influx (Fig.S10F). The influx of Ca^{2+} induced by I1 is independent of AMPAR channels, shown by the unchanged Ca^{2+} influx curves with the cyanquixaline (CNQX) inhibitor (Fig.S10G).

Discussion

Since there is no information about oligomers *ex vivo*, we compared the end product of our *in vitro* oligomer preparation, the L2 fibrils with the *ex vivo* Lewy fold. The latter closely resembles L2 but differs in notable aspects. The Lewy fold fibrils occur only as single filaments, whereas L2 consists of three filaments (Fig.S11A). There are also variations in the fold of individual filaments. Specifically, the Lewy fold features a near 180˚ turn at G84, in contrast to L2's approximately 90˚ turn. Additionally, the turn at G73-is nearly 90˚ in the Lewy fold and about 160° in L2, leading to a concave bend at G51 in the Lewy fold versus a convex bend at the same position in L2 (Fig.S11B).

Despite these differences, the similarities between the Lewy fold and L2 fibrils are striking. Both share the T59-arc (β2-β3) that is common structural kernel in multiple αS fibrils[4]. There are also similarities in other segments, including the interactions between β1 and β4 as well as the organization of β5 (Fig.S11C). These similarities make the I1 oligomer from the *in vitro* L2 fibril preparation a remarkable model for studying the assembly of structural features present in brain extracted αS fibrils.

The I1 structure is distinct from non-toxic oligomers which are helical and more dynamic such as the dynamic helical tetramer and those stabilized by EGCG (epigallocatechin-3-gallate)[11,31,32]. Additionally, I1 is distinct from stable lipoprotein particles formed by helical αS[33]. While non-toxic oligomers interact with lipid bilayers in an unspecific

manner[11,31], the I1 N-terminus contacts lipids via an amphipathic helix and many segments contact the hydrophobic bilayer core. This interaction pattern may influence the cellular fate of αS aggregates because the lipid binding sites also act as recognition motifs for protein quality control, such as for heat shock proteins (V37-K43 in αS)[34,35] and ubiquitination (K21, K23, K32, K34 in αS)[36].

The I1 model suggests that aggregation prone regions (APRs) are among the first to adopt β-strands in the aggregation process. Identified through factors like hydrophobicity, solubility[37], and mutagenesis studies[38], APRs include the Y39-S42 master controller region, and the K45-E57 segment housing several familial mutations linked to Parkinson's disease[37,39]. In I1 residues in these segments adopt β-strands (β1 and β2 in Fig.3A) and engage in tertiary and backbone interactions with other APRs (β3 and β4 in Fig.3A). All of these segments are consistent with those that lend energetic stability to αS fibrils[39]. Additionally, lipid bound dimers reveal helix breaks at V40 and K60[40], suggesting that the destabilization of the functional helix in these segments may steer the molecule toward amyloid aggregation. G84-V95 is a hydrophobic segment; however, instead of a β-strand, it forms a lipid bound loop in I1 (Fig. 4B). This deviation is attributed to its relatively lower aggregation propensity and higher solubility than the other segments[37].

Biophysical commonalities, namely, the ability to disrupt membranes[6] and the presence of anti-parallel β-sheet[7–9,41] have emerged among toxic amyloid oligomers. Consistent with this, the lipid defects caused by I1 (Fig.4C-E and S10A, B) are reminiscent of edge pores observed with amyloid-β oligomers[42,43] that impair membrane integrity. This impairment has been extensively studied as a mechanism involving increased influx of cations in the context of various amyloid oligomers[6]. The resulting increased influx of cations such as Ca^{2+} is an integral step in the apoptosis signaling pathway which is responsible for the death dopaminergic neurons[44].

Anti-parallel β-strands in toxic oligomers were first observed in bulk measurements[7,8] and have since been reported to occur at different residues, featuring varied topologies such as a β-hairpin (L38-A53)[45] or a steric zipper (K80-A91)[9]. Given the polymorphism observed in αS fibrils, multiple intermediate structures can be expected, evidenced by different residues participating in the AP β-strands. However, commonalities in the aggregation pathway are evident, as, similar to I1 oligomers (Movie S1), amyloid-β oligomers have also been reported to undergo a 90° turn in a β-hairpin during fibril formation[21]. The presence of β-arcs in most known fibrils suggests a common assembly pathway through a hairpin-to-arc transition.

The conservation of the β-arc structural kernel at T59 in a vast number of αS fibrils (Fig.1B and S12) suggests that contacts like the I1 AP domain could be initiators of aggregation for these polymorphs. Tetrameric oligomers modelled from these polymorphs can accommodate I1 type AP β-strands in their otherwise distinct structural folds (Fig.S12B) and the formation of such domains appears to be energetically favorable (Fig.S13B). This suggests that I1 type AP domains may be at the heart of a common folding pathway for fibril polymorphs with a β-arc at T59 (Fig.S13A). The β-arc at G67 is implicated in the formation of MSA-type fibrils (Fig.S12A)[4]. Exploring αS oligomers preceding the G67 arc could offer insights into the fibrillogenesis of MSA-type fibrils.

Here we have localized with atomic scale precision, the occurrence of AP β-strands in a toxic αS tetramer. We demonstrate that aggregates containing these AP β-strands precede the formation of fibrillar intermediates, and their transition into a fibril like β-arc is essential for fibril elongation. The observation that the tetramer is in contact with hydrophobic lipid chains and results in detrimental cation influx highlights its potential role in disrupting the integrity of biological membranes, such as those of presynaptic termini, where αS is known to be enriched[46]. Findings here underscore that the tetramer structural models can serve as a basis to investigate genesis, polymorphism and therapeutic intervention for fibrils with similar sub-structures, like the brain extracted PD/ DLB fibrils. The presence of AP strands may be an early step in triggering the amyloid aggregation process, which has been implicated in various neurodegenerative diseases.

References

1. Spillantini, M. G. *et al.* α-synuclein in Lewy bodies. *Nature* vol. 388 839–840 Preprint at https://doi.org/10.1038/42166 (1997).
2. MG, S. *et al.* Filamentous alpha-synuclein inclusions link multiple system atrophy with Parkinson's disease and dementia with Lewy bodies. *Neurosci Lett* **251**, 205–208 (1998).
3. Lövestam, S. *et al.* Disease-specific tau filaments assemble via polymorphic intermediates. *Nature 2023 625:7993* **625**, 119–125 (2023).
4. Sawaya, M. R., Hughes, M. P., Rodriguez, J. A., Riek, R. & Eisenberg, D. S. The expanding amyloid family: Structure, stability, function, and pathogenesis. *Cell* **184**, 4857–4873 (2021).
5. Yang, Y. *et al.* Structures of α-synuclein filaments from human brains with Lewy pathology. *Nature 2022 610:7933* **610**, 791–795 (2022).

6. Limbocker, R. *et al.* Characterization of Pairs of Toxic and Nontoxic Misfolded Protein Oligomers Elucidates the Structural Determinants of Oligomer Toxicity in Protein Misfolding Diseases. *Acc Chem Res* (2023) doi:10.1021/ACS.ACCOUNTS.3C00045.

7. Lorenzen, N. *et al.* The Role of Stable α-Synuclein Oligomers in the Molecular Events Underlying Amyloid Formation. (2014) doi:10.1021/ja411577t.

8. Chen, S. W. *et al.* Structural characterization of toxic oligomers that are kinetically trapped during α-synuclein fibril formation. *Proc Natl Acad Sci U S A* **112**, E1994–E2003 (2015).

9. Chen, S. W. *et al.* Structure-Toxicity Relationship in Intermediate Fibrils from α-Synuclein Condensates. *J Am Chem Soc* **146**, 10537 (2024).

10. Grazia Spillantini, M. *et al.* Filamentous α-synuclein inclusions link multiple system atrophy with Parkinson's disease and dementia with Lewy bodies. *Neurosci Lett* **251**, 205–208 (1998).

11. Fusco, G. *et al.* Structural basis of membrane disruption and cellular toxicity by a-synuclein oligomers. *Science (1979)* **358**, 1440–1443 (2017).

12. Lashuel, H. A. *et al.* α-synuclein, especially the parkinson's disease-associated mutants, forms pore-like annular and tubular protofibrils. *J Mol Biol* **322**, 1089–1102 (2002).

13. Cremades, N. *et al.* Direct observation of the interconversion of normal and toxic forms of α-synuclein. *Cell* **149**, 1048–1059 (2012).

14. Winner, B. *et al.* In vivo demonstration that α-synuclein oligomers are toxic. *Proc Natl Acad Sci U S A* **108**, 4194–4199 (2011).

15. Danzer, K. M. *et al.* Different Species of α-Synuclein Oligomers Induce Calcium Influx and Seeding. *Journal of Neuroscience* **27**, 9220–9232 (2007).

16. Diao, J. *et al.* Native α-synuclein induces clustering of synaptic-vesicle mimics via binding to phospholipids and synaptobrevin-2/VAMP2. *Elife* **2013**, (2013).

17. Nakamura, K. *et al.* Direct membrane association drives mitochondrial fission by the Parkinson disease-associated protein alpha-synuclein. *J Biol Chem* **286**, 20710–20726 (2011).

18. Davidson, W. S., Jonas, A., Clayton, D. F. & George, J. M. Stabilization of α-Synuclein secondary structure upon binding to synthetic membranes. *Journal of Biological Chemistry* **273**, 9443–9449 (1998).

19. Shahmoradian, S. H. *et al.* Lewy pathology in Parkinson's disease consists of crowded organelles and lipid membranes. *Nat Neurosci* **22**, 1099–1109 (2019).

20. Comellas, G., Lemkau, L. R., Zhou, D. H., George, J. M. & Rienstra, C. M. Structural intermediates during α-synuclein fibrillogenesis on phospholipid vesicles. *J Am Chem Soc* **134**, 5090–5099 (2012).

21. Chandra, B. *et al.* Major Reaction Coordinates Linking Transient Amyloid-β Oligomers to Fibrils Measured at Atomic Level. *Biophys J* **113**, 805 (2017).

22. Sarkar, B. *et al.* Significant Structural Differences between Transient Amyloid-β Oligomers and Less-Toxic Fibrils in Regions Known To Harbor Familial Alzheimer′s Mutations. *Angewandte Chemie International Edition* **53**, 6888–6892 (2014).

23. Antonschmidt, L. *et al.* Insights into the molecular mechanism of amyloid filament formation: Segmental folding of α-synuclein on lipid membranes. *Sci Adv* **7**, eabg2174 (2021).

24. Frieg, B. *et al.* The 3D structure of lipidic fibrils of α-synuclein. *Nature Communications 2022 13:1* **13**, 1–10 (2022).

25. Frieg, B. *et al.* The 3D structure of lipidic fibrils of α-synuclein. *Nature Communications 2022 13:1* **13**, 1–10 (2022).

26. Nimerovsky, E. *et al.* Modest Offset Difference Internuclear Selective Transfer via Homonuclear Dipolar Coupling. *Journal of Physical Chemistry Letters* **13**, 1540–1546 (2022).

27. Luo, W. & Hong, M. Determination of the oligomeric number and intermolecular distances of membrane protein assemblies by anisotropic 1H-driven spin diffusion NMR spectroscopy. *J Am Chem Soc* **128**, 7242–7251 (2006).

28. Zijlstra, N., Blum, C., Segers-Nolten, I. M. J., Claessens, M. M. A. E. & Subramaniam, V. Molecular Composition of Sub-stoichiometrically Labeled α-Synuclein Oligomers Determined by Single-Molecule Photobleaching. *Angewandte Chemie International Edition* **51**, 8821–8824 (2012).

29. Weisenburger, S. *et al.* Cryogenic optical localization provides 3D protein structure data with Angstrom resolution. *Nature Methods 2017 14:2* **14**, 141–144 (2017).

30. Mazal, H., Wieser, F. F. & Sandoghdar, V. Deciphering a hexameric protein complex with Angstrom optical resolution. *Elife* **11**, (2022).

31. Xu, L., Bhattacharya, S. & Thompson, D. On the ubiquity of helical α-synuclein tetramers. *Physical Chemistry Chemical Physics* **21**, 12036–12043 (2019).

32. Wang, W. *et al.* A soluble α-synuclein construct forms a dynamic tetramer. *Proc Natl Acad Sci U S A* **108**, 17797–17802 (2011).

33. Eichmann, C. *et al.* Preparation and Characterization of Stable α-Synuclein Lipoprotein Particles. *J Biol Chem* **291**, 8516 (2016).

34. Wentink, A. S. *et al.* Molecular dissection of amyloid disaggregation by human HSP70. *Nature 2020 587:7834* **587**, 483–488 (2020).

35. Schneider, M. M. *et al.* The Hsc70 disaggregation machinery removes monomer units directly from α-synuclein fibril ends. *Nature Communications 2021 12:1* **12**, 1–11 (2021).

36. Nonaka, T., Iwatsubo, T. & Hasegawa, M. Ubiquitination of α-synuclein. *Biochemistry* **44**, 361–368 (2005).

37. Doherty, C. P. A. *et al.* A short motif in the N-terminal region of α-synuclein is critical for both aggregation and function. *Nature Structural & Molecular Biology 2020 27:3* **27**, 249–259 (2020).

38. Chlebowicz, J. *et al.* Saturation mutagenesis of α-synuclein reveals monomer fold that modulates aggregation. *Sci Adv* **9**, eadh3457 (2023).

39. Louros, N., Schymkowitz, J. & Rousseau, F. Mechanisms and pathology of protein misfolding and aggregation. *Nature Reviews Molecular Cell Biology 2023 24:12* **24**, 912–933 (2023).

40. Schwarz, T. C. *et al.* High-resolution structural information of membrane-bound α-synuclein provides insight into the MoA of the anti-Parkinson drug UCB0599. *Proc Natl Acad Sci U S A* **120**, e2201910120 (2023).

41. Serra-Batiste, M. *et al.* Aβ42 assembles into specific β-barrel pore-forming oligomers in membrane-mimicking environments. *Proc Natl Acad Sci U S A* **113**, 10866–10871 (2016).

42. Matthes, D. & de Groot, B. L. Molecular dynamics simulations reveal the importance of amyloid-beta oligomer β-sheet edge conformations in membrane permeabilization. *Journal of Biological Chemistry* **299**, 103034 (2023).

43. Ciudad, S. *et al.* Aβ(1-42) tetramer and octamer structures reveal edge pores as a mechanism for membrane damage. doi:10.1101/759472.

44. Dong, X. X., Wang, Y. & Qin, Z. H. Molecular mechanisms of excitotoxicity and their relevance to pathogenesis of neurodegenerative diseases. *Acta Pharmacologica Sinica 2009 30:4* **30**, 379–387 (2009).

45. Yu, H., Han, W., Ma, W. & Schulten, K. Transient β-hairpin formation in α-synuclein monomer revealed by coarse-grained molecular dynamics simulation. *J Chem Phys* **143**, 243142 (2015).

46. Maroteaux, L., Campanelli, J. T. & Scheller, R. H. Synuclein: a neuron-specific protein localized to the nucleus and presynaptic nerve terminal. *Journal of Neuroscience* **8**, 2804–2815 (1988).

Methods

Protein production and tagging with ATTO647N dye

Expression of αS was performed in the *E. coli* strain BL21(DE3). Unlabeled, uniformly ^{15}N-, uniformly ^{13}C- and uniformly ^{15}N, ^{13}C-labeled αS was performed in modified minimal medium. ^{15}N-NH_4Cl was used as the nitrogen source and $^{13}C_6$-D-glucose as carbon source, and the protein purification was performed as described before[47]. Mutant αS with an additional C-terminal cysteine (A140C) was generated by PCR-based site-directed

mutagenesis (QuikChange 2, Agilent Technologies). The cysteine mutant was tagged with ATTO647N dye by overnight incubation on ice with a two-fold molar excess of the maleimide in phosphate buffered saline (PBS), pH 7.4. Excess dye was removed by gel filtration on a Superdex 75 16/60 HiLoad column (Cytiva). Successful tagging was verified by electrospray ionization mass spectrometry. All protein samples were finally dialyzed against 50mM HEPES pH 7,4, 100mM NaCl. The final protein concentration was adjusted to 0.3 mM.

Intermediate 1 sample preparation for MAS NMR

Aggregation of αS was according to the protocol in Antonschmidt et.al.[23]. Monomeric αS in 50 mM HEPES and 100 mM NaCl (pH7.4) was centrifuged for 1 hour at 55,000 rpm (TLA-100.3 rotor in an Optima MAX-TL ultracentrifuge, Beckman Coulter) at 4°C to remove any large aggregates. The supernatant was decanted and added to a solution of SUVs (small unilamelar vesicles) and NaN_3 (0.02 weight %) to obtain a final protein concentration of 70 µM and a molar Lipid/Protein ratio of 10:1 or 5:1. The mixture was sonicated in cycles for 30s (20 kHz) with 30 minutes of quiescence between sonication at 37°C using a Q700-110 sonication device, with a Microplate Horn Assembly (431MPX) and a Compact Recirculating Chiller (4900-110, all QSonica). The aggregation was monitored with Thioflavin-T fluorescence until the reading exceeded the background value (~6-8 a.u.) by ~2 units at which point a pellet of I1 was collected via ultracentrifugation. Maintaining temperature at ~4°C during centrifugation and rotor packing, and ~16°C for MAS NMR measurements ensured batch-to-batch reproducibility and stability (Fig.S1).

ThioflavinT (ThT) fluorescence of the samples was monitored continuously by taking aliquots from the aggregating solution in the sonicator and mixing with a working solution composed of 50 mM glycine buffer at pH 8.5 and 2.5 µM ThT. Measurements were done on the Varian Cary Eclipse fluorescence spectrometer. Fluorescence was excited at 446 nm and emission was recorded from 460 to 560 nm at room temperature. The aggregating solution was vortexed atleast once before collecting an aliquot for the ThT measurement. For a single 1.3 mm rotor, about ~ 8 mL of 70 µM αS was aggregated in batches of 1.65 mL. Batch to batch differences in the length of the lag phase were accounted for by measuring ThT fluorescence for each batch independently, and the increase in fluorescence was relative to the initial value of that specific batch. This approach resulted in samples with repeatable spectra (Fig. S1D) and the ThT fluorescence measurements for the samples prepared for this study are shown in Fig. S1E.

As soon as 2 units increase in fluorescence was detected, samples were placed on ice and centrifuged at 55,000 rpm (TLA-100.3 rotor in an Optima MAX-TL ultracentrifuge, Beckman Coulter) for 1 hour at 4°C. After decanting the supernatant, the pellet was washed with 5 mM HEPES (pH 7.4 and subsequently centrifuged (10 min, 65,000 rpm, 10°C) twice, each time removing excess moisture. Samples were packed into ssNMR rotors by cutting off the bottom of the centrifuged tube and centrifuging (at 4°C) the pellet directly into the rotor through a custom-made filling device made from a truncated pipette tip. The rotor was centrifuged in an ultracentrifuge packing device for 30 min at 24,000 rpm in an SW 32 Ti rotor in an Optima L-80 XP Ultracentrifuge (both Beckman Coulter) at 4°C for packing the pellet[48]. After this step, for 1.3 mm rotors, excess water was pushed out of the rotor by pushing on the bottom rubber seal before closing the rotor. All rotor packing steps were performed in the cold room, as far as possible, using tweezers, to prevent the intermediate from changing states.

Preparation of SUVs

SUVs were produced as previously described in Antonschmidt et.al.[23] Briefly, POPC and the sodium salt of POPA, obtained from Avanti Polar Lipids, were dissolved in chloroform and mixed to obtain a 1:1 molar ratio of both lipids. The solvent was evaporated under a nitrogen stream and lyophilized overnight. The lipid film was rehydrated with 50 mM HEPES, pH 7.4 and 100 mM NaCl buffer to a total lipid concentration of 3 mM. The solution was sonicated at 37 kHz for four cycles of 10 mins sonication and 10 minutes rest and filtered through a 0.22 µm syringe filter to obtain SUVs.

ssNMR

All measurements were performed on Intermediate 1 composed of u-^{13}C,^{15}N-labeled αS. 3D (H)CANH, (HCO)CA(CO)NH, (H)CONH, (H)CO(CA)NH and (HCA)CB(CA)NH experiments [49] for protein sequence assignment and 3D H(H)NH (z-mixing) experiments for lipid-protein contacts were acquired on an 800-MHz Bruker Avance III HD spectrometer at a magnetic field of 18.8 T equipped with a 1.3-mm magic-angle spinning (MAS) HCN probe and MAS at 55 kHz and an estimated sample temperature of 16°C. The cooling gas flow was set at ~ 1500 liters per hour and temperature of the cooling gas was set to 235 K. The delays for scalar carbon-carbon transfers were set based on the T2′ values of 20 ms for Cα and 45 ms for C′ as shown in Table S2.1. For backbone assignment experiments, an Intermediate 1

sample aggregated with 10:1 L:P was used. Amine side chains for Q62 and N65 were assigned based on contacts from H(H)NH and corresponding C' assignments from (H)CONH and (H)Ca(CO)NH spectra.

Chemical shifts for Cα, CO, Cβ, H_N and N_H were inputted in TALOS+ to obtain predictions on secondary structure and dihedral backbone angles[50]. Secondary structure was confirmed with secondary chemical shift differences between Cα, Cβ resonances and their random coil values calculated according to Schwarzinger et.al.[51] Chemical shift perturbations between fibril and I1 were calculated according to equations in Williamson et.al.[52] from ^{13}C-^{13}C and (H)CaNH spectra:

$$\text{Average CSP} = \sqrt{\frac{1}{4}\left[(\delta C\alpha)^2 + (2.37\delta C\beta)^2 + (0.47\delta Co)^2 + (1.30\delta NH)^2\right]}.$$

The H(H)NH pulse sequence used for proton-proton z-mixing measurements is similar to that reported by Najbauer et.al. where longitudinal mixing drives proton-proton mixing between the protein and mobile lipid and water molecules[53]. To eliminate spectral overlap between protein side-chain resonances and lipid protons, a T_2 filter and a J-filter of 3 ms have been added after the proton excitation pulse.

Partial side-chain assignments were obtained from (H)CCH experiments with ^{13}C-^{13}C RFDR mixing of 1.3 ms. Long range contacts were obtained from H(H)NH and H(H)CH experiments with ^{1}H-^{1}H RDFR mixing of 0.5 ms. [54] These experiments were acquired on a 1200 MHz Bruker Avance NEO spectrometer at a magnetic field of 28.2 T equipped with a 1.3-mm magic-angle spinning (MAS) HCN probe and MAS at 55 kHz and an estimated sample temperature of 16°C. For these measurements, 100 mM Cu-EDTA was added to the sample in the rotor to an estimated final concentration of 40 mM for sensitivity enhancement [55]. This shortened the recycle delay from 1.6 s to 0.6 s without causing changes to the (h)CaNH spectrum.

The (H)N(H)(H)NH MODIST spectra was acquired on a 1200 MHz Bruker Avance NEO spectrometer at a magnetic field of 28.2 T equipped with a 1.3 mm magic-angle spinning (MAS) HCN probe and MAS of 55,555 Hz with 3.46 ms of ^{1}H-^{1}H MODIST mixing[26]. The sample contained Cu-EDTA at 40 mM. The temperature of the cooling gas was set to 245 K with a flow of 1000 liters per hour. The spectral widths were 40 ppm for ^{1}H and 38 ppm on ^{15}N. ^{1}H and ^{15}N hard pulses were 100 kHz and 58.8 kHz. The spectra were recorded for 8 days for the 100% labelled sample and 17 days for the 50% labelled sample.

606 The 2D ^{13}C-^{13}C DARR spectrum with a mixing time of 20 ms was acquired on an 850
607 MHz Avance III spectrometer with a 3.2 mm MAS HCN probe at a magnetic field of 20.0 T
608 and MAS at 17 kHz.

609 For all spectra 13.75 kHz MISSISSIPPI water suppression [56] (100 to 200 ms), 12.75
610 kHz Swf-TPPM proton decoupling during acquisition of the indirect dimension [57] and 10 kHz
611 WALTZ-16 heteronuclear decoupling during acquisition was used.

612 Spectra were acquired in short blocks of 12-21 hrs for linear drift correction [58]. The
613 drift-corrected blocks were then averaged and processed as one spectrum in Bruker Topspin 3
614 or 4. Window functions used to process spectra were exponential and quadratic sine. Spectra
615 were analyzed using CcpNmr Analysis.

616 The stability of the sample during solid-state nuclear magnetic resonance (ssNMR)
617 measurements was monitored by (H)NH spectrum recorded intermittently between blocks of
618 3D experiment acquisitions. Measurements were halted when the intensity of the spectrum
619 began to reduce, or new peaks appeared in the (H)NH spectrum. A new sample was prepared
620 for further measurements and the reproducibility of the (H)NH spectrum for I1 samples is
621 shown in (Fig. S1). I1 samples were remarkably stable (Fig. S1) even after 21 days at 55 kHz
622 magic angle spinning (MAS) and an estimated sample temperature of 16°C. This can be
623 attributed to lack of free monomer available to polymerize I1 into higher order aggregates
624 (Fig. S1), relatively slow diffusion in the densely packed pellet in the ssNMR rotor and a
625 sample temperature in the magnet which was much lower than that used for aggregation
626 (37°C).

627 Spectra were processed and analyzed on CCPN Analysis[59] and Topspin 4.0.7 (Bruker,
628 AXS GmBH). Signal to noise ratios were determined in Sparky[60].

629 **Transmission Electron Microscopy**

630 An I1 sample was resolubilized from a MAS ssNMR rotor and dissolved in 5%
631 glycerol and 5mM HEPES (pH 7.4) buffer. This was diluted 1:80 times and used to blot TEM
632 grids. Samples were bound to a glow discharged carbon foil covered 400 mesh copper grid.
633 Samples were stained with 1% uranyl acetate aqueous solution and evaluated at room
634 temperature using a TALOS L120C (Thermo Fisher Scientific). Images were analyzed in
635 ImageJ software[61].

Center-band Only Detection of Exchange (CODEX) under Dynamic Nuclear Polarization Conditions (DNP)

Isolated I1 sample was mixed with TEMTriPol in ^{13}C-depleted d_8-Glycerol, D_2O and H_2O (60:30:10 vol%) to a final concentration of 15 mM final concentration. This was packed in a 3.2 mm rotor and flash frozen by plunging in liquid nitrogen. The fibril sample was exchanged with glycerol until the mass indicated 60% vol% of glycerol. Then AMUPOL powder was added to a concentration of 30 mM before mixing and plunge freezing the rotor. 395 GHz of microwave irradiation was applied that resulted in a 4 times enhancement for I1 and 30 times enhancement for the fibril sample. All CODEX experiments were measured on a 600 MHz Bruker Avance III HD spectrometer, and a 3.2 mm low temperature (LT) HCN MAS probe at 8 kHz MAS. Principle of using CODEX to count the oligomeric numbers is discussed in detail in previous literatures[27,62,63].

Photobleaching measurements at room temperature

ATTO647N bound to A140C αS was aggregated as described before with wild type (WT) αS at a ratio of 1:3 ATTO-αS: WT. Once isolated, the sample was packed in a 1.3 mm rotor and an ^{15}N-^{1}H fingerprint spectra confirmed that the sample indeed was structurally similar to I1 (Fig.S4).

The proteins were diluted to a stock solution of 50 nM in 10 mM HEPES and 10% glycerol at pH 7.8 (working buffer). The protein was further diluted into the working buffer containing 5% poly-vinyl alcohol (PVA) to obtain a final concentration of ~20 pM. Then, 4 µl of this diluted solution was spin-coated onto a plasma-cleaned mirror-enhanced substrate, which was prepared in-house[64]. Finally, the sample was immediately loaded into our custom-built cryogenic microscope[64].

Upon inserting the sample into our custom-built cryogenic microscope, we applied a vacuum for 5 minutes to immobilize the molecules. After releasing the vacuum, we started acquiring videos from multiple fields of view (FOV) at room temperature (RT). The sample was illuminated with a 645 nm wavelength laser at 2 mW in a wide-field (WF) mode using an air objective (Mitutoyo 100X, 0.9 NA). Each FOV (80x80 µm) was recorded at a frame rate of 10 Hz for up to 8 minutes, a time point which shows complete photobleaching in the FOV. Next, we localized and clustered each molecule in the FOV to extract their intensity levels over time. The intensity time traces were then fitted using the DISC algorithm to extract the

number of intensity steps per molecule[65]. Here, we used a critical value of 15, and the minimum number of points per cluster was set to 15. To avoid any sources of artifact in the final analysis resulting from low signal-to-noise traces or traces that included high blinking events, we filtered the intensity time traces with a signal-to-noise ratio (SNR) above 5. The output from this analysis (1421 time traces) was then plotted as a histogram and fitted with a binomial model to extract the labeling efficiency or the stoichiometry of the intermediate oligomers. The binomial distribution described as $P(k) = \binom{n}{k} p^k (1-p)^{n-k}$, where P is the probability that an oligomer contains k labeled subunits, n is the total number of monomers per oligomer and p is the labeling efficiency. Here we obtain the fit parameter (p), theoretical labeling efficiency, as a function of the total number of monomers (n) as depicted in Figure S4F. We plotted the labeling error ($\frac{|\text{fitted labeling efficiency} - \text{experimental value}|}{\text{experimental value}}$)as a function of monomers per oligomer (red curve) and we find that the best model is a tetramer (black arrow in Fig.S4F). Similarly, the residual of the fit indicate that tetramer is the best model (orange curve, Fig.S4F).

Cryogenic polarization measurements (polarCOLD)

The sample was prepared and imaged using the same instrument as in the fluorescence photobleaching experiment. For polarCOLD, the chamber was completely evacuated to a pressure of 1.6×10^{-6} mbar and then cooled down to 4.3 K using liquid helium. The setup was then allowed to stabilize for 1-2 hours to minimize drift during recordings. Subsequently, the sample was illuminated with a 20 mW laser in WF mode, utilizing the same laser source and microscope objective. The emission signal was split into two channels using a polarized beam splitter, enabling the recording of a polarization time trace, as described before[30]. After localizing and clustering each point spread function (PSF), we extracted the polarization time trace, which was then fitted using the DISC algorithm to determine the number of polarization states per molecule. The number of identified polarization states (dipole orientation) in each PSF corresponds to the number of labeled monomers per oligomer, as the dipole orientation at 4K of each fluorophores is random but fixed (see Fig.S4G). This, in turn, allow us to annotate each fluorophore over time and localize it with high precision beyond the diffraction limit by clustering their coordinates accordingly (Fig.2E-H). Then, a 2D super-resolved image is reconstructed by assigning a 2D Gaussian function to each localized fluorophore with a width given by the respective localization precision. These super-resolved images demonstrate different projections of the protein molecules within the sample. The output of the number of

polarizations (from 962 traces) was plotted as a histogram (Fig.2D), yielding results similar to those obtained from the photobleaching steps experiment.

Cell viability assay

SH-SY5Y cells were grown in 45% modified eagle media supplemented with L-glutamine (2 mM), HAM's F-12 nutrient mixture (45%), fetal bovine serum (10%) and non-essential amino acids (1%). Cells were grown on Poly-D-lysine coated dishes and one day before treatment, cells were plated in a 96-well plate at a density of 2x 10^4 cells/ well. Samples consisting of the intermediate 1, fibrils or monomers were added to the cells at concentrations defined in Fig.1 and incubated at 37°C for 20-24 hours. At the end of the treatment period XTT (2,3-bis(2-methoxy-4-nitro-5-sulfophenyl)-5-carboxanilide-2H-tetrazolium) and electron coupling reagent (ThermoFisher Scientific) were added and incubated for another 4 hours before reading absorbance at 450 nm and 660 nm. Results are presented after subtraction of blank absorbance at 450 nm and well as background at 660 nm from the test absorbance at 450 nm.

Calcium flux and cell death assay

SH-SY5Y cells were plated in a 96 well plate at a density of 2x 10^4 cells/ well. The next day, media was aspirated and media containing 3 μM Fluo-4 was added. Cells were incubated at 37°C for 1 hour. Fluo-4 AM containing media was removed and replaced with phenol red free DMEM supplemented with Glutamine and 10% FBS. The plate was incubated for another 10 minutes to load cells with Fluo-4 and ensure complete de-esterification of Fluo-4 AM. CNQX (cyanquixaline) diluted in media or equivalent amount of media for control was added to cells to a concentration of 5 μM. Then either I1 in 5mM HEPES, or equivalent amount of buffer, monomer, fibrils or ionomycin were added to the cells at a concentration of 0.6 μM. Plate was equilibrated in the BioTEK plate reader at 37°C for 15 minutes before measurements began. Fluorescence was excited at 488 nm and measured at 530 nm using a filter cube. In another set of well, after the overnight incubation, media is replaced with phenol red free media. Either I1 in 5mM HEPES, or equivalent amount of buffer, monomer or fibrils were added to the cells at a concentration of 0.6 μM. As a dead cell control, cells were lysed with 10% SDS. Then propidium iodide was added at a concentration of 50 μg/ml. Fluorescence was read in parallel to Fluo-4 with monochromator based fluorescence module on the BioTEK reader at excitation and emission wavelengths of 535 nm and 622 nm respectively.

Liposomal proton flux assay

A pH-based proton flux assay was adapted from a previous protocol used for viroporins[66]. Liposomes were made by combining 10 mg of Escherichia coli polar lipid extract (Avanti Polar Lipids) dissolved in chloroform, valinomycin solution in ethanol and methanol in a glass tube. The solvents were evaporated under continuous nitrogen gas and a thin film was obtained. The films were dissolved in chloroform again and dried down under a nitrogen stream and were left overnight in the lyophilizer to remove any solvent trace. The films were then resuspended in strongly buffered internal liposome buffer (26 mM potassium citrate, 17 mM citric acid, 28 mM sodium citrate, 25 mM K_2HPO4, 25 mM Na_2HPO_4, 6 mM NaN_3; pH 7.7) to form liposomes which were then extruded 11 times through 0.2 M polycarbonate membrane. Buffer was exchanged on a PD-10 column (GE Health Sciences) such that the external liposome buffer was a weak buffer (4% v/v IVB, 117 mM KCl, 117 mM NaCl, 6 mM NaN_3, pH 7.7).

Every tested sample contained 5 mg/mL lipids, and 0.1 μM valinomycin as a potassium ionophore. The external pH was decreased by the addition of 1M HCl under continuous fast stirring. Once the pH had stabilized, 0.6 μM of I1 in 5mM HEPES or equivalent amount of buffer without I1 was added and pH was recorded every second. The proton uncoupler carbonyl cyanide m-chlorophenylhydrazone (CCCP) was added to determine the buffering capacity of the liposomes.

CYANA Modeling

Contacts from Supplementary Table S1 were used for the CYANA[67] calculation with 250 structures and 80000 steps. Parallel in-register hydrogen bonds were assumed for segments that show chemical shift similarity (<0.7 ppm average CSP) and high fidelity in long range contacts with the L2 fibril for stretches V31-G51, E57-Q62, and G67-K80. Dihedral angles with good confidence from the TALOS+ prediction were used with one standard deviation with the exception of loop regions, where the limits for the dihedral angles for the loops were increased to three standard deviations. This resulted in the structures with a target function of ~5.

Molecular Dynamic (MD) Simulations

To produce an atomistic I1 structure model with restrained MD simulations the core of the α-Synuclein L2 fibril structure (8A4L, residue 33-83) was taken. The N-terminal part was removed. For a N- and C-terminally extended I1 structure model, residues 16-33 & 83-99 were taken from the micelle-bound α-Synuclein monomer structure (1XQ8) and fitted on

763 residue Thr33 & GLu83, respectively. Three different tetrameric intermediate 1 AP domain
764 morphologies (’open’, bowl’ and ‘barrel’) are derived by MD simulations with distance
765 restraints in a water box (Table S1 and Fig.S8, S9). In all simulation systems, the titratable
766 amino acids were protonated according to their standard protonation states at pH 7, while also
767 taking into account the solvent exposure and electrostatic interactions with neighboring polar
768 groups. Thus, aspartic and glutamic side-chains were simulated with negative charge and all
769 histidine side-chains were set to neutral. All lysine side-chains were simulated as positively
770 charged[68]. The N- and C-termini of the truncated α-Synuclein molecules were capped with
771 acetyl and N-methyl groups, respectively. All production runs were preceded by a multi-step
772 equilibration of the system. The protein part was separately energy minimized in water.
773 Bilayers patches with a ratio of 1;1 ratio of POPC and POPA lipids and a water slab of 3.5
774 mm thickness of top and bottom of the bilayer were prepared using the CHARMM-GUI[69]
775 webserver. The membrane patch was relaxed for 1 ns at 300 K. Next, the α-Synuclein
776 structures were either embedded into the lipid bilayer or positioned close to it (see
777 orientations 1/8 in Fig.S7) in several different orientations. Subsequently, and if not states
778 otherwise, Na+ and Cl− ions (ionic strength: 150 mM) were added in the aqueous phase of the
779 periodic simulation box. The total simulation size varied and amounted to roughly 68k to
780 230k atoms (around 200 to 500 lipids, 13k to 54k waters) with varied depending on the used
781 α-Synuclein model (short and long construct).

782

783 For the short construct of the open morphology in different orientations, each case was
784 simulated as triplicates of MD simulations with 1000 ns length. For the analysis based on
785 experimental lipid contacts the first 750 ns of each simulation data were discarded. For
786 different morphologies in the bilayer, each case was run in triplicates of 500 ns. The first 250
787 ns of the simulation data discarded for the analysis based on experimental distance restraints
788 and lipid contacts. For the analysis of lipid contacts and intermolecular distances all
789 simulation sets per case were pooled. For the longer constructs, a total of 22 MD simulations
790 of embedded structures were run for 100 ns with distance restraints and an additional 500 ns
791 without restraints to collect data that are evaluated against experimental measurements.

792 The GROMACS 2022 simulation[70,71] software package was used to set up, carry out and
793 analyze the MD simulations. Settings for production runs were chosen as follows: The long
794 range electrostatic interactions were treated using the Particle Mesh Ewald (PME) method[72,73]
795 . Bonds in protein and lipid molecules were constrained using the P-LINCS algorithm[74].

Water molecules were constrained using SETTLE algorithm[75]. Neighbor lists were updated with the Verlet list scheme[71,76] . For production runs, the simulated systems were kept at a temperature of 300 K by applying the velocity-rescaling [77] algorithm. Initial velocities for the production runs were taken according to the Maxwell-Boltzmann distribution at 300 K. The pressure was held constant by using the Parrinello-Rahman barostat[78] with a semi-isotropic coupling in the xy-plane.

All simulations with the CHARMM36m[79,80] protein force field utilized the CHARMM36 lipid[81] parameters together with the CHARMM-modified[82] TIP3P water model. The integration time step was set to 2 fs. The neighbor lists for non-bonded interactions were updated every 20 steps. Real-space electrostatic interactions were truncated at 1.2 nm. The van der Waals interactions were switched off between 1.0 to 1.2 nm and short-range electrostatic interactions were cut-off at 1.2 nm. For pressure coupling the scheme of Parrinello-Rahman[78] was used to hold the system at a pressure of 1 bar ($\tau = 5$).

Structure and MD simulation renderings were produced with Chimera[83] and ChimeraX[84].

Solution NMR

^{15}N-labeled αS was mixed with 50 mM HEPES (pH 7.4) and 100 mM NaCl to obtain samples with 10% D_2O and 100 μM 2,2-dimethyl-2-silapentane-5-sulfonate sodium. Experiments were recorded on a Bruker 700-MHz spectrometer (Avance III HD with CP-TCI HCND probe with z-gradient) at 288 K. ^{1}H-^{15}N-HSQC spectra were acquired using 3-9-19 watergate for water suppression using 256 increments in the indirect dimension and a relaxation delay of 1.2 s. Assignment of the ^{1}H-^{15}N-HSQC spectrum was done by comparison to BMRB entries 16300, 16904, and 18857.

Data availability

Assigned chemical shift data for αS Intermediate 1 were deposited in the BMRB under the accession number 52283. Additional data related to this paper may be requested from the authors.

References for Methods and Supplementary Information

47. Hoyer, W. *et al.* Dependence of α-Synuclein Aggregate Morphology on Solution Conditions. *J Mol Biol* **322**, 383–393 (2002).

48. Böckmann, A. *et al.* Characterization of different water pools in solid-state NMR protein samples. *Journal of Biomolecular NMR 2009 45:3* **45**, 319–327 (2009).

49. Barbet-Massin, E. *et al.* Rapid Proton-Detected NMR Assignment for Proteins with Fast Magic Angle Spinning. *J Am Chem Soc* **136**, 12489–12497 (2014).

50. Shen, Y., Delaglio, F., Cornilescu, G. & Bax, A. TALOS+: a hybrid method for predicting protein backbone torsion angles from NMR chemical shifts. *Journal of Biomolecular NMR 2009 44:4* **44**, 213–223 (2009).

51. Schwarzinger, S. *et al.* Sequence-dependent correction of random coil NMR chemical shifts. *J Am Chem Soc* **123**, 2970–2978 (2001).

52. Williamson, M. P. Using chemical shift perturbation to characterise ligand binding. *Prog Nucl Magn Reson Spectrosc* **73**, 1–16 (2013).

53. Najbauer, E. E. *et al.* Probing Membrane Protein Insertion into Lipid Bilayers by Solid-State NMR. *ChemPhysChem* **20**, cphc.201800793 (2018).

54. Andreas, L. B. *et al.* Structure of fully protonated proteins by proton-detected magic-angle spinning NMR. *Proceedings of the National Academy of Sciences* **113**, 9187–9192 (2016).

55. Wickramasinghe, N. P., Kotecha, M., Samoson, A., Past, J. & Ishii, Y. Sensitivity enhancement in 13C solid-state NMR of protein microcrystals by use of paramagnetic metal ions for optimizing 1H T1 relaxation. *Journal of Magnetic Resonance* **184**, 350–356 (2007).

56. Zhou, D. H. & Rienstra, C. M. High-performance solvent suppression for proton detected solid-state NMR. *Journal of Magnetic Resonance* **192**, 167–172 (2008).

57. Bennett, A. E., Rienstra, C. M., Auger, M., Lakshmi, K. V. & Griffin, R. G. Heteronuclear decoupling in rotating solids. *J Chem Phys* **103**, 6951 (1998).

58. Najbauer, E. E. & Andreas, L. B. Correcting for magnetic field drift in magic-angle spinning NMR datasets. *Journal of Magnetic Resonance* **305**, 1–4 (2019).

59. Skinner, S. P. *et al.* CcpNmr AnalysisAssign: a flexible platform for integrated NMR analysis. *J Biomol NMR* **66**, 111–124 (2016).

60. Lee, W., Tonelli, M. & Markley, J. L. NMRFAM-SPARKY: enhanced software for biomolecular NMR spectroscopy. *Bioinformatics* **31**, 1325 (2015).

61. Schneider, C. A., Rasband, W. S. & Eliceiri, K. W. NIH Image to ImageJ: 25 years of image analysis. *Nature Methods 2012 9:7* **9**, 671–675 (2012).

62. Xue, K., Dervisoglu, R., Sowa, H. & Andreas, L. B. Centerband-Only Detection of Exchange NMR with Natural-Abundance Correction Reveals an Expanded Unit Cell in Phenylalanine Crystals. *ChemPhysChem* **21**, 1622–1626 (2020).

63. Williams, J. K., Shcherbakov, A. A., Wang, J. & Hong, M. Protonation equilibria and pore-opening structure of the dual-histidine influenza B virus M2 transmembrane proton channel from solid-state NMR. *Journal of Biological Chemistry* **292**, 17876–17884 (2017).

64. Böning, D., Wieser, F. F. & Sandoghdar, V. Polarization-Encoded Colocalization Microscopy at Cryogenic Temperatures. *ACS Photonics* **8**, 194–201 (2021).

65. White, D. S., Goldschen-Ohm, M. P., Goldsmith, R. H. & Chanda, B. Top-down machine learning approach for high-throughput single-molecule analysis. *Elife* **9**, (2020).

66. Pielak, R. M., Schnell, J. R. & Chou, J. J. Mechanism of drug inhibition and drug resistance of influenza A M2 channel. *Proc Natl Acad Sci U S A* **106**, 7379–7384 (2009).

67. Güntert, P. & Buchner, L. Combined automated NOE assignment and structure calculation with CYANA. *Journal of Biomolecular NMR 2015 62:4* **62**, 453–471 (2015).

68. Teixeira, V. H., Vila-Viçosa, D., Reis, P. B. P. S. & MacHuqueiro, M. PKa Values of Titrable Amino Acids at the Water/Membrane Interface. *J Chem Theory Comput* **12**, 930–934 (2016).

69. Jo, S., Kim, T., Iyer, V. G. & Im, W. CHARMM-GUI: A web-based graphical user interface for CHARMM. *J Comput Chem* **29**, 1859–1865 (2008).

70. Pronk, S. *et al.* GROMACS 4.5: a high-throughput and highly parallel open source molecular simulation toolkit. *Bioinformatics* **29**, 845 (2013).

71. Abraham, M. J. *et al.* GROMACS: High performance molecular simulations through multi-level parallelism from laptops to supercomputers. *SoftwareX* **1–2**, 19–25 (2015).

72. Darden, T., York, D. & Pedersen, L. Particle mesh Ewald: An N·log(N) method for Ewald sums in large systems. *J Chem Phys* **98**, 10089–10092 (1993).

73. Essmann, U. *et al.* A smooth particle mesh Ewald method. *J Chem Phys* **103**, 8577–8593 (1995).

74. Hess, B. P-LINCS: A parallel linear constraint solver for molecular simulation. *J Chem Theory Comput* **4**, 116–122 (2008).

75. Miyamoto, S. & Kollman, P. A. Settle: An analytical version of the SHAKE and RATTLE algorithm for rigid water models. *J Comput Chem* **13**, 952–962 (1992).

76. Verlet, L. Computer "Experiments" on Classical Fluids. I. Thermodynamical Properties of Lennard-Jones Molecules. *Physical Review* **159**, 98 (1967).

77. Bussi, G., Donadio, D. & Parrinello, M. Canonical sampling through velocity rescaling. *Journal of Chemical Physics* **126**, 14101 (2007).

78. Parrinello, M. & Rahman, A. Polymorphic transitions in single crystals: A new molecular dynamics method. *J Appl Phys* **52**, 7182–7190 (1981).

79. Best, R. B. *et al.* Optimization of the additive CHARMM all-atom protein force field targeting improved sampling of the backbone φ, ψ and side-chain χ1 and χ2 Dihedral Angles. *J Chem Theory Comput* **8**, 3257–3273 (2012).

80. Huang, J. *et al.* CHARMM36m: an improved force field for folded and intrinsically disordered proteins. *Nature Methods 2016 14:1* **14**, 71–73 (2016).

81. Klauda, J. B. *et al.* Update of the CHARMM All-Atom Additive Force Field for Lipids: Validation on Six Lipid Types. *Journal of Physical Chemistry B* **114**, 7830–7843 (2010).

82. MacKerell, A. D. *et al.* All-atom empirical potential for molecular modeling and dynamics studies of proteins. *Journal of Physical Chemistry B* **102**, 3586–3616 (1998).

83. Pettersen, E. F. *et al.* UCSF Chimera—A visualization system for exploratory research and analysis. *J Comput Chem* **25**, 1605–1612 (2004).

84. Pettersen, E. F. *et al.* UCSF ChimeraX: Structure visualization for researchers, educators, and developers. *Protein Science* **30**, 70–82 (2021)

Acknowledgments

We thank M. Wegstroth for the preparation of isotope-labeled α-Synuclein stock solutions and K. Giller for the preparation of dye labeled α-Synuclein. We thank L.Kopecny for taking negative-stain electron micrographs. We thank Mr. J. Schimpfhauser, Mr. J Bienert and Dr. V. N. Belov from the facility for Synthetic Chemistry at the Max Planck Institute for Multidisciplinary Sciences, Göttingen for synthesizing the TEMTriPol-1 radical.

This work was supported by the Max Planck Society (to CG, VaS and BLdG) and the Deutsche Forschungsgemeinschaft (DFG, German Research Foundation) under Germany's Excellence Strategy-EXC 2067/1-390729940 (to CG) and the Emmy Noether program to LBA (project number: 397022504).

Author contributions

Intermediate1 samples were prepared by VS and LA. NMR experiments were performed by VS, LA, KMT, KX, EN. Cell experiments performed by VS and MN. Liposomal proton flux assay was performed by VS and MS. Fluorescence measurements were performed and analyzed by HM and FW. MD simulations were performed and analyzed by DM. Conceptualization and methodology by BLdG, CG, LBA, VS and LA. SB oversaw protein expression and purification. VaS oversaw fluorescence measurements. VS prepared the figures and wrote the initial draft. BLdG, CG, and LBA supervised the project. All authors contributed to the writing of the manuscript.

Competing interests

No competing interests to declare.

Supplementary Information is available for this paper.

Correspondence and requests for materials should be addressed to C.G. at cigr@mpinat.mpg.de and L.B.A at land@mpinat.mpg.de and BLdG at bgroot@mpinat.mpg.de

Supplementary Files

This is a list of supplementary files associated with this preprint. Click to download.

- I1supplementaryfigurestables.pdf
- SIGuide.docx
- MovieS1.mp4
- MovieS2.mp4
- MovieS3.mp4